$LiCo_{1-y}M_yO_2$ positive electrodes for rechargeable lithium batteries: II. Nickel substituted materials grown by the citrate method

C.M. Julien[a,*], A. Amdouni[b], S. Castro-Garcia[c], M. Selmane[a], S. Rangan[a]

a Institut des Nano-Sciences de Paris, Université Pierre et Marie Curie, CNRS-UMR7588, Campus Boucicaut, 140 rue de Lourmel, 75015 Paris, France

b UR Physico-Chimie des Matériaux Solides, Département de Chimie, Faculté des Sciences de Tunis, Campus Universitaire, 1060 Tunis, Tunisia

c Departamento Quimica Fundamental e Industrial, Universidade A Coruna, 15071 A Coruna, Spain

Materials Science and Engineering: B

Volume 128, Issues 1–3, 15 March 2006, Pages 138–150

Received 11 October 2005, Accepted 28 November 2005, Available online 18 January 2006

DOI: 10.1016/j.mseb.2005.11.042

Abstract

The layered $LiCo_{1-y}Ni_yO_2$ microcrystalline powders were synthesized by a sol–gel method using citric acid as a chelating agent in the range $0.2 \leq y \leq 0.8$. Submicron-sized particles of the precursor were obtained at temperature below 400 °C and microcrystalline powders were grown by thermal treatment at 700 °C for 5 h in air. The carboxylic-based acid functioned such as a fuel, decomposed the homogeneous precipitate of metal complexes at low temperature, and yielded the free impurity

$LiCo_{1-y}Ni_yO_2$ single-phases suitable for electrochemical applications. The synthesized products were characterized by structural, spectroscopic and thermal analyses. FT-IR measurements provide information on the growth process and the final local environment in the cationic sublattice of $LiCo_{1-y}Ni_yO_2$ solid solution. The electrochemical performance of the synthesized products in rechargeable Li cells was evaluated using non-aqueous solution 1 M $LiPF_6$ in EC-DMC as electrolyte. The electrochemical features of a series of $LiCo_{1-y}Ni_yO_2$ compounds ($0.2 \leq y \leq 1.0$) are discussed in relation with their synthesis procedure and substitutive amount. The substitution of Ni^{3+} for Co^{3+} in $LiCo_{1-y}Ni_yO_2$ for $y = 0.75$ shows improvement of the specific capacity at ca. 187 mAh/g upon 32 cycles.

Keywords

Lithium secondary batteries; Lithium nickel–cobalt oxides; Sol–gel method; Chelating agent; Citric acid; Lithium diffusivity

1. Introduction

Lithiated transition-metal oxides with high oxidation state of metal ions have attracted attention for their technological use as positive electrodes of rechargeable lithium batteries because lithium ions are electrochemically extracted and inserted with high reversibility [1], [2], [3], [4], [5], [6], [7], [8], [9], [10],[11] and [12]. These compounds show higher operating voltages than the conventional 3 V systems (V_2O_5, MnO_2, etc.). The most studied cathodes in this series are the layered $LiMO_2$ (M = Ni, Co) and the spinel $LiMn_2O_4$ Solid solution of lithium nickel–cobalt oxides, $LiCo_{1-y}Ni_yO_2$ ($0 \leq y \leq$ l), are also candidate materials. They exhibit several advantages in comparison with the parent end-members $LiCoO_2$ and $LiNiO_2$; the effects of substitution of Co for Ni are interesting in terms of the structural and electrochemical properties and from the economic viewpoint [4]. Exhibiting a lower potential, $LiCo_{1-y}Ni_yO_2$ oxides are less active for an organic electrolyte oxidation and prevent the nickel dioxide formation associated with a strong exothermic reaction. Therefore the use of solid solution system, $LiCo_{1-y}Ni_yO_2$, can be the way to optimize alternative electrode materials, since it has a high discharge capacity (>140 mAh/g) and offers a superior cycling behavior compared to other systems [6], [7], [8], [9], [10] and [11].

From a structural point of view, Li*M* O_2 oxides crystallize in a layered α-$NaFeO_2$-type ($R\bar{3}m$ symmetry) structure in which Li and M cations fill alternately the octahedral sites in the oxygen cubic close packing [1]. $LiCo_{1-y}Ni_yO_2$ materials, which are isostructural with the layered oxide end-compounds, show better crystallinity than lithiated nickelates, for which the non-stoichiometry ($Li_{1-z}Ni_{1+z}O_2$), due to the excess of nickel ions sitting in the interlayer space, is well known [13]. With increasing Co content in the solid solution, the trigonal distortion of the crystal lattice increases and the deviation from the stoichiometry of lithium nickelate decreases [6], [7], [8] and [9]. The standard high-temperature (HT) $LiCo_{1-y}Ni_yO_2$ powders have usually been prepared by the solid-state reaction in which hydroxides or carbonates are calcined at about 800–900 °C for a prolonged period [14] and [15] along with multiple grinding operation.

Research works in this area have focused the attention on new synthesis routes for low-temperature crystallized oxides (LT–Li*M*O_2), which showed some promise in improving the cycle life of rechargeable lithium batteries [16], [17], [18] and [19]. Recently, Pereira-Ramos [20] has critically discussed the impact afforded by low-temperature techniques especially sol–gel synthesis and precipitation techniques on the electrochemical behavior of the oxide materials as prepared. Solution preparative techniques allow a better mixing of the elements and thus a better reactivity of the mixture to obtain purer reaction products. Lower reaction temperature and shorter reaction time are then possible to yield a compound of high homogeneity and high specific area. Moreover, these methods make use of lower calcination temperatures resulting in particles of smaller size and a highly strained lattice. Sol–gel is gradually attracting the attention of the electrochemistry community as a versatile way for the preparation of intercalation electrodes [21]. In the sol–gel process, a solid phase is formed through gelation of a colloidal suspension. Drying of the gel can then give “dry gel” (xerogel) state and subsequent heat treatment can be used to remove unreacted organic residues, stabilize the gel, density it, or introduce crystallinity [22], [23], [24] and [25].

In this paper, we report on the low-temperature synthesis of positive electrode materials $LiCo_{1-y}Ni_yO_2$using a wet chemical technique, namely citric acid-assisted sol–gel method. We present the physical properties of synthesized $LiCo_{1-y}Ni_yO_2$ materials investigated by several characterization techniques, such as thermal analysis (TG-DTA), X-ray powder diffraction (XRD), scanning electron microscopy (SEM), and Fourier transform infrared (FT-IR) spectroscopy. The low-temperature procedure provides microcrystalline, layered-structured compounds with uniform submicron-sized

particles. The electrochemical properties of these oxides have been studied by coupling it as cathode with Li anode and a non-aqueous electrolyte.

2. Experimental

2.1. Synthesis of $LiCo_{1-y}Ni_yO_2$ samples

The $LiCo_{1-y}Ni_yO_2$ ($0.2 \leq y \leq 0.8$) powders were synthesized according to the procedure shown in the flowchart (Fig. 1). The sol–gel process is based on the preparation of a colloidal suspension, a sol, and its transition into a gel from which the microcrystalline material can be obtained. Starting from molecular precursors, an oxide network is obtained via inorganic polymerization reactions in solution. This method involves the mixing of acetates of the metals, Ni and Co, with the complexing agent, citric acid, in an aqueous medium. Citric acid, $HOC(COOH)(CH_2COOH)_2$, acts such as a fuel during the formation process of transition-metal oxide powders, decomposes the homogeneous precipitate of metal complexes at low temperature, and yields the free impurity $LiCo_{1-y}Ni_yO_2$ compounds. Stoichiometric amounts of acetate hydrates of Li, Co and Ni (Fluka, purum p.a. grade) were dissolved in triple distilled water and mixed well with an aqueous solution of citric acid (Fluka, MicroSelect grade). The (COOH) carboxylic acid groups present in the complexing agent $C_4H_8O_7$ could form a chemical bond with the metal ions and produce viscous resin on evaporation of the solvent, which is usually called as precursor. The resultant solution was then evaporated off at 80 °C with magnetic stirring for about 6 h until a sol was formed. The resulting xerogel was transparent violet in color. Finally, the products referred as precursor powders were formed by heating the gel at 120 °C. It is a fluffy dark brownish powder. The decomposed powders were slightly ground and further heated to 400–700 °C in air to obtain single-phase microcrystalline $LiCo_{1-y}Ni_yO_2$. The products obtained were fine grained materials of submicron-sized particles.

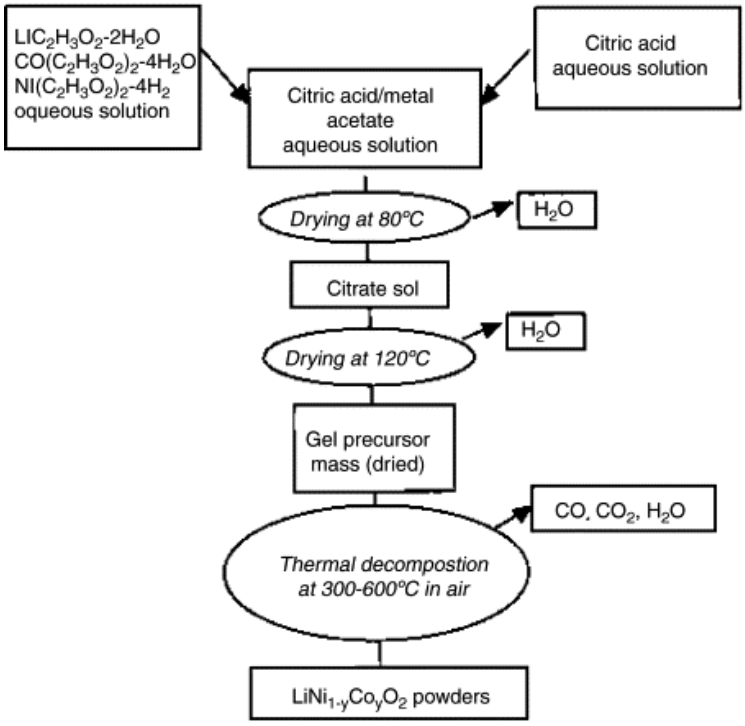

Fig. 1. Synthetic procedure of microcrystalline $LiCo_{1-}yNiyO_2$ powders by the citric acid-assisted sol–gel method.

2.2. Instruments

The thermal decomposition behavior of the gel precursors was examined by means of thermal gravimetry (TG) and differential thermal analysis (DTA) using a Netzsch analyzer (model STA 409). XRD patterns were obtained with a Philips X-ray diffractometer (model PW1830) using nickel-filtered Cu Kα radiation (λ = 1.5406 Å). The diffraction patterns were taken at room temperature in the range of $10° < 2\theta < 80°$ using step scans. The step size and the scan rate were set at 0.1 and 0.2°/min, respectively. The particle morphologies of the materials were examined by scanning electron microscopy (SEM, Cambridge Instruments, Stereoscan 120).

FT-IR absorption spectra were recorded using a Bruker IFS113v interferometer at a spectral resolution 2 cm^{-1}. In the studied region (100–700 cm^{-1}), this vacuum bench apparatus was equipped with a 3.5 μm thick beamsplitter, a globar source, and a DTGS-PE far-infrared detector. Samples were ground to fine powders painted onto polyethylene slab which is a transparent substrate in the studied spectral range.

2.3. Electrochemical measurements

Electrochemical studies were carried out on the synthesized products fired at 700 °C in order to test their suitability as cathode-active materials in high-voltage lithium-containing batteries. The above tests were performed to measure quantitatively the capacity and the cyclability of the synthesized products. The laboratory-scale Li||$LiCo_{1-y}Ni_yO_2$ cells were housed in a Teflon laboratory-cell hardware employing a non-aqueous Li^+ ion conducting organic electrolyte as follows. The electrolyte was prepared by dissolving 1 M $LiPF_6$ in ethylene-dimethylene carbonate (EC-DMC) mixture. The cathode-active materials were pressed onto an expanded aluminium microgrid at a pressure of 500 MPa. This procedure yields circular pellet electrodes of 10 mm diameter. The pellets were then dried at 120 °C in air. Glass paper soaked in electrolyte was used as the membrane separator between the cathode and the anode. Electrochemical measurements were carried out using a Mac-Pile system in the galvanostatic mode. Quasi open-circuit voltage profiles were measured using intermittent charging as follows. A current of 0.14 mA/cm^2 was supplied for 1 h, corresponding to a lithium extraction of about 0.01 mol from 1 mol of the electrode material. This was followed by a relaxation time of 0.5 h before the next charging started. The charging–discharging processes were monitored in the potential range between 2.5 and 4.2 V, corresponding to a depth-of-discharge (DOD) of $\Delta x \approx 0.6$. The apparent lithium content of the charge–discharge compounds was estimated using the current passed and the mass of the electrode material.

3. Results and discussion

3.1. Thermal analysis

Fig. 2 shows the TG-DTA curves of $LiCo_{1-y}Ni_yO_2$ xerogels. The weak endothermic effect associated with a small weight loss of about 5% for $T < 200$ °C are attributed to departure of residual water. A strong exothermic peak appears at 316 °C after the departure of the remaining water molecule. This exothermic effect corresponds to the combustion of citric acid and acetate ions xerogel. More than half of the weight loss occurs during this stage because of a violent oxidation–decomposition reaction. It appeared that citric acid acts as a fuel in the pyrolysis of the gel precursor, accelerating the decomposition of acetate ions. It was reported that chelating agent (carboxylic-

based acid) provides combustion heat for calcination in the synthesis of oxide powders [26] and [27]. The gel precursor was self-burning once ignited, because the decomposed acetate ions acted as an oxidizer. The weight loss in the temperature range 330–400 °C corresponds to the decomposition of the remaining organic constituents, which is accompanied by a wide exothermic peak at 380 °C. Eventhough the crystallization starts below 400 °C; thus well-crystallized and pure phases have been obtained at 600 °C. While the pyrolysis at this stage was very complicated, it could be presumed that the last weak exothermic at ca. 380 °C in the DTA curves corresponds to the crystallization of the $LiCo_{1-y}Ni_yO_2$ phases. XRD studies after the last effect indicate that very intimately mixed cobalt and nickel lithium oxides reacted together. Thus, $LiCo_{1-y}Ni_yO_2$ compounds have been formed.

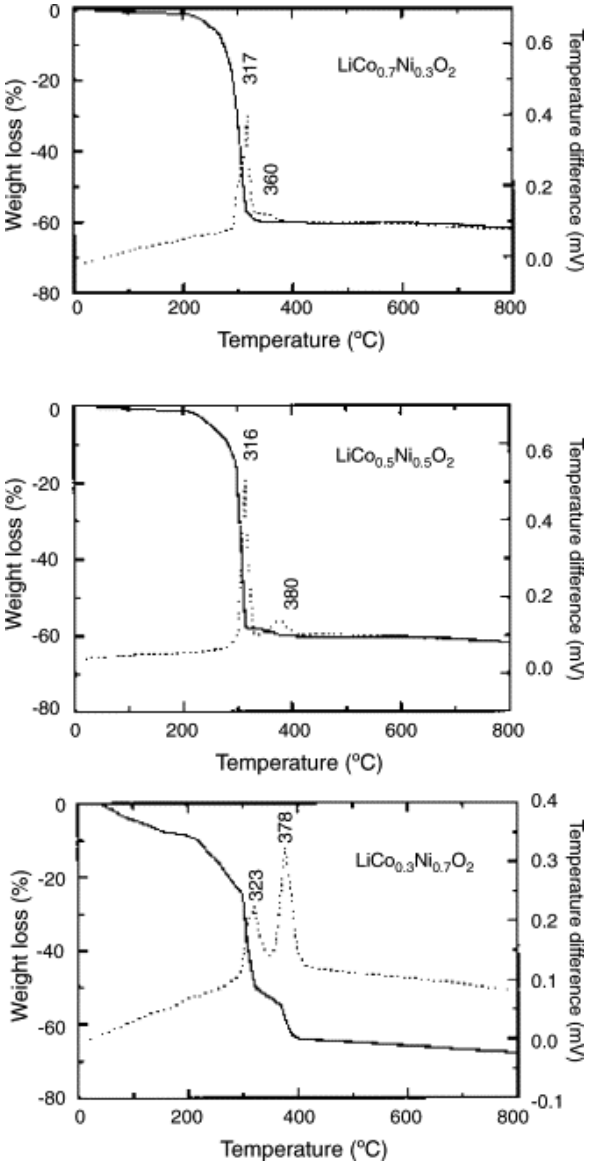

Fig. 2. TG-DTA curves of the $LiCo_{1-y}Ni_yO_2$ ($0.3 \leq y \leq 0.7$) xerogels. Measurements were carried out at a heating rate of 10 °C/min with oxygen flow.

3.2. Structure and morphology

Fig. 3 shows the X-ray diffraction patterns of $LiCo_{0.4}Ni_{0.6}O_2$ powders as a function of the calcination temperature in air. XRD results concerning the dried $LiCo_{1-y}Ni_yO_2$ xerogel heated for 5 h at 400, 500, 600 and 700 °C are reported in Table 1. The XRD peaks gradually sharpen with increasing firing temperature, which indicates an increase of crystallinity as may occur from growth of grain size, ordering of local structure, and/or release of lattice strain. The crystallographic parameters (*a* and *c* hexagonal setting) for $LiCo_{0.4}Ni_{0.6}O_2$ powders are reported with the existence of residuals. Below heating at 700 °C, we have identified the presence of impurities such as NiO, Co_2O_3, Ni_2O_3, Ni_2O_3H and $Ni(OH)_2$–$0.75H_2O$. At 700 °C, an impurity free $LiCo_{0.4}Ni_{0.6}O_2$ compound is formed after 5 h heating. The corresponding XRD diagram shows narrower peaks at this temperature due a better crystallinity. It can be remarked that the single-phase microcrystalline $LiCo_{0.4}Ni_{0.6}O_2$ was not formed at 400 °C even for long heating times, e.g. 3 days. From these data, there is evidence that oxidation of Ni^{2+} into Ni^{3+} is more difficult than oxidation of Co^{2+} into Co^{3+}.

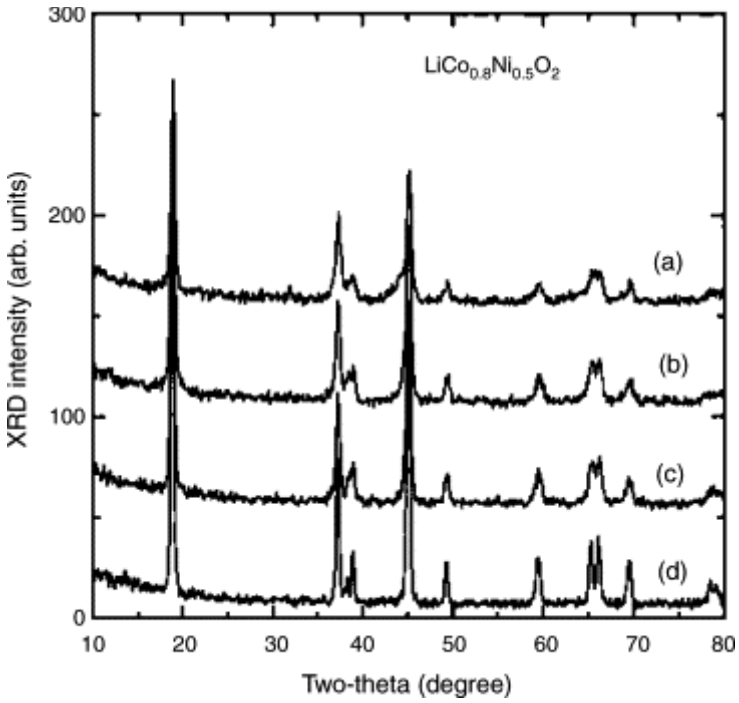

Fig. 3. X-ray diffraction patterns of $LiCo_{0.4}Ni_{0.6}O_2$ powders as a function of the calcination temperature in air. (a) 400 °C, (b) 500 °C, (c) 600 °C, and (d) 700 °C.

Table 1. X-ray diffraction data for xerogels $LiCo_{0.4}Ni_{0.6}O_2$ heated in the temperature range 120–700 °C. The *a* and *c* parameters correspond to the hexagonal cell. (d) and (n) means that impurities are detected or not

T (°C)	*a* (Å)	*c* (Å)	NiO	Ni_2O_3	CO_2O_3	$Ni(OH)_2$–H_2O	$Ni(OH)_2$
120	2.860	14.104	d	d	d	d	d
400	2.840	14.116	d	d	n	d	d
500	2.845	14.130	d	d	n	d	d
600	2.849	14.132	n	n	n	d	n
700	2.852	14.139	n	n	n	n	n

.

Fig. 4 displays the XRD patterns of $LiCo_{1-y}Ni_yO_2$ microcrystalline powders calcined at 700 °C for 5 h in air. The XRD patterns indicate a phase pure material; no peaks attributed to a second phase are observed. These XRD diagrams appear to be similar to those reported in the literature for $LiCo_{1-y}Ni_yO_2$[7]. They are dominated by a strong Bragg peak located at ca. $2\theta = 19°$ and Bragg peaks with medium intensity at 36° and 44°. Considering the intensity and position of the Bragg peaks, it is well known that patterns of the rhombohedral unit-cell ($R\bar{3}m$ space group) can be indexed in the hexagonal system. These materials exhibit, as their parent $LiMO_2$, the classical layered structure generally found for the most $LiMO_2$ oxides isomorphous with α-$NaFeO_2$. Lithium ions are inserted in octahedral sites between $(Ni,Co)O_2$ slabs built up of edge-sharing $(Ni,Co)O_6$ octahedra.

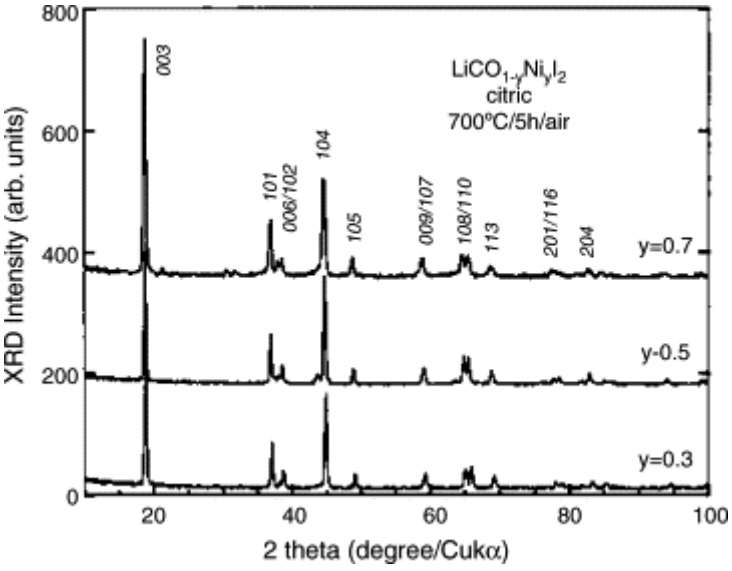

Fig. 4. X-ray diffraction diagrams of $LiCo_{1-y}Ni_yO_2$ ($0.3 \leq y \leq 0.7$) microcrystalline materials calcined at 700 °C for 5 h in air.

Table 2 shows the results of the structural analysis of $LiCo_{1-y}Ni_yO_2$ precursor powders calcined at 800 °C for 5 h in air. Unit-cell parameters were determined in the hexagonal sitting by a least-squares method using 11 diffraction lines. The reliability index *R* was estimated to be in the range $0.02 \leq R \leq 0.04$. An interesting point to emphasize is the variation of the (*c*/*a*) ratio which characterizes the layered structure (i.e. anisotropy) [11]. This criterion establishes the deviation from the hexagonal-close-packed structure when $(c/a) < 4.94$ for $y = 0$ and $(c/a) < 4.99$ for $y = 1$. Fig. 5a and b shows the variation of hexagonal unit-cell parameters with nickel concentration *y* in $LiCo_{1-y}Ni_yO_2$ compounds. These results show that crystallographic parameters of $LiCo_{1-y}Ni_yO_2$ vary almost linearly between those of the end-members $LiNiO_2$ and $LiCoO_2$ suggesting that synthesized $LiCo_{1-y}Ni_yO_2$ products belong to the solid solution. For nickel substitutive, the α-$NaFeO_2$-type structure is almost ideal. The cobalt-rich compounds have the smaller crystallographic parameter *c* (Fig. 5b) which is related to the interlayer metal–metal spacing. Its monotonous decrease with decreasing cobalt content is the result of the difference in ionic radii between Co^{3+} and Ni^{3+} cations. Co^{3+} (0.685 Å) has a smaller ionic radius than Ni^{3+} (0.70 Å) [28]. In the same way, the cationic difference explains the increase in the metal–metal intralayer distance (*a* parameter) as shown in Fig. 5a.

Table 2. XRD results obtained on $LiCo_{1-y}Ni_yO_2$ powders calcined at 700 °C for 5 h from xerogels prepared by the citric acid-assisted method The lattice parameters are given assuming the $R\bar{3}m$ symmetry (hexagonal setting). The distance metal–oxygen $d_{(M-O)}$ within the slab is also given.

y(Ni)	Lattice parameters				Intensity ratio of $I_{(0\,0\,3)}/I_{(1\,0\,4)}$	$d_{(M-O)}$ (Å)
	a (Å)	*c* (Å)	*c*/*a*	*V* (Å^3)		
0.20	2.825	14.092	4.9883	97.39	1.705	1.977
0.30	2.833	14.109	4.9802	97.99	1.687	1.971
0.40	2.836	14.117	4.9778	98.23	1.666	1.966
0.50	2.844	14.128	4.9677	98.85	1.589	1.963
0.60	2.852	14.139	4.9576	99.46	1.509	1.959
0.70	2.858	14.151	4.9535	100.00	1.367	1.955
0.75	2.866	14.161	4.9410	100.23	1.304	1.955
0.80	2.868	14.165	4.9390	100.48	1.255	1.961

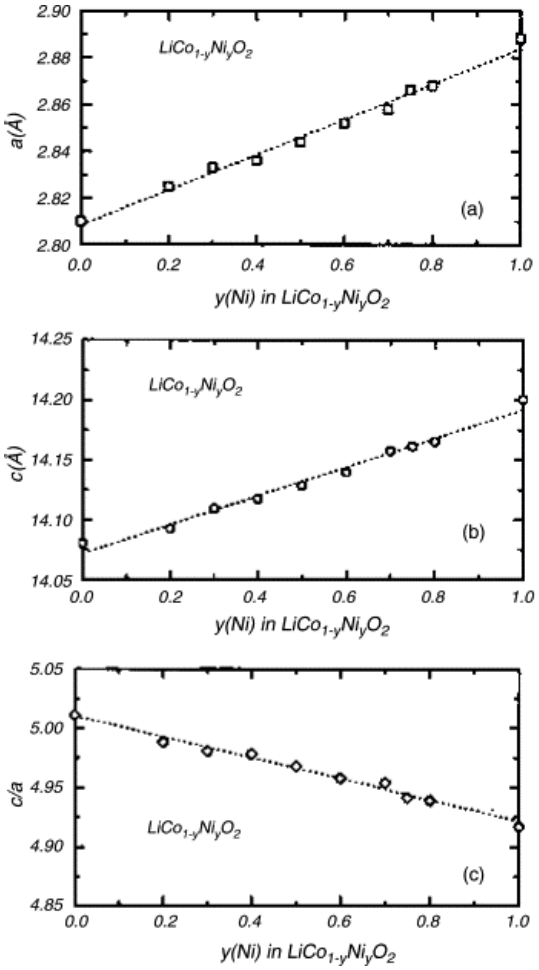

Fig. 5. The variation of hexagonal unit-cell parameters with cobalt concentration *y* in $LiCo_{1-y}Ni_yO_2$ ($0.2 \le y \le 0.8$) solid solution. Dashed line represents the crystallographic parameter vs. *y* relationship without cation mixing effect.

In the case of $LiCo_{1-y}Ni_yO_2$ phases, special attention has to be drawn to the existence of extra cations in the lithium layers impeding structural disturbances. Disorder of this nature, which is called cation mixing, i.e. the partial mixing between Ni^{3+} and Li^{+} ions in the predominantly lithium layer, can seriously degrade electrochemical features of the positive electrodes such as rechargeable capacity and Li ion diffusion. Fig. 5c shows the variation of the *c*/*a* ratio with the nickel content in $LiCo_{1-y}Ni_yO_2$ compounds. The slope of (*c*/*a*) versus *y* relationship indicates that the Ni^{3+} substitution for Co^{3+} occurs almost without cation mixing for $y < 0.2$. The changes in layer occupancy have a direct effect on the X-ray intensity ratios such as $I_{(0\,0\,3)}/I_{(1\,0\,4)}$ and $I_{(0\,0\,6,\,1\,0\,2)}/I_{(1\,0\,1)}$ ratios, which are considered to be indicators of the ordering of lithium and other transition metal (Ni and/or Co) [29] and [30]. When the integrated intensity ratio of (0 0 3) to (1 0 4) peaks was below 1.2, either the (1 0 8) and (1 1 0) peaks or (0 0 6) and (1 0 2) peaks, become difficult to distinguish from each other. As shown in Fig. 4, $LiCo_{1-y}Ni_yO_2$ powders grown by sol–gel process method exhibit XRD patterns with quite well-defined doublets (0 0 6, 1 0 2) and (1 0 8, 1 1 0) when calcined at 700 °C for

5 h because the presence of cobalt stabilizes the structure in a strictly two-dimensional fashion. However, the nickel-rich compound $LiCo_{0.2}Ni_{0.8}O_2$ exhibits some structural deviations which are attributed to the cation mixing (Table 2). These structural features favor good reversibility of the deintercalation and intercalation reaction [3]. The (*c*/*a*) ratio very different from the critical value 4.90 and the splitting of the (0 0 6) and (1 0 2) as well as (1 0 8) and (1 1 0) diffraction lines indicate, as far as XRD measurements are concerned, the stabilization of the two-dimensional structure and an ordered distribution of lithium and transition-metal ions in the lattice. XRD results confirm the formation of pure phase, but the question of the local cationic order will be re-examined below by spectroscopic measurements.

The degree of crystallinity of the $LiCo_{1-y}Ni_yO_2$ products, i.e. particle shape, crystallite size, domain size, was examined by XRD and SEM. At first, the crystallite size, δ, is estimated from the XRD pattern with the aid of the Scherrer's formula

$$\delta = 0.9\frac{\lambda}{B\cos\theta},$$

where λ is the X-ray wavelength (λ = 1.5406 Å), and B is the FWHM of the XRD peak in radians. The crystallite sizes of powders grown by the citrate route (*T* calcinations 700 °C) are found in the range 21–25 nm for $0.2 \leq y \leq 0.8$.

Fig. 6 presents the evolution of the morphology of $LiCo_{1-y}Ni_yO_2$ $LiCo_{0.6}$ powders as a function of the calcination process. It is seen, that products fired at 400 °C show agglomerated particles, while powders calcined at 600 °C start to be well formed with grains of regular shape and submicron size. Fig. 7 shows the typical scanning micrographs of $LiCo_{1-y}Ni_yO_2$ (y = 0.3, 0.5, and 0.7) samples fired at 700 °C in air for 5 h. These pictures reveal that the gel precursors fired at 700 °C develop well-crystallized powders with homogeneous morphologies. The domain size becomes quite small; an average diameter below 1 μm was obtained with a fairly narrow particle size distribution range. The grains are almost connected and ensure the high surface area.

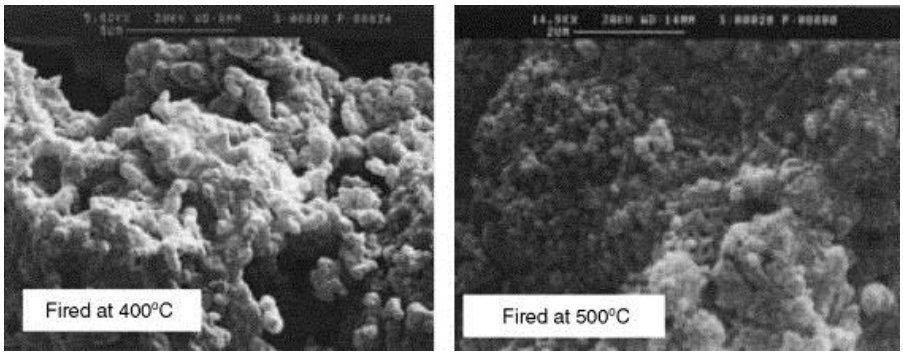

Fig. 6. Typical SEM micrographs of $LiCo_{0.4}Ni_{0.6}O_2$ sample as a function of the calcination temperature.

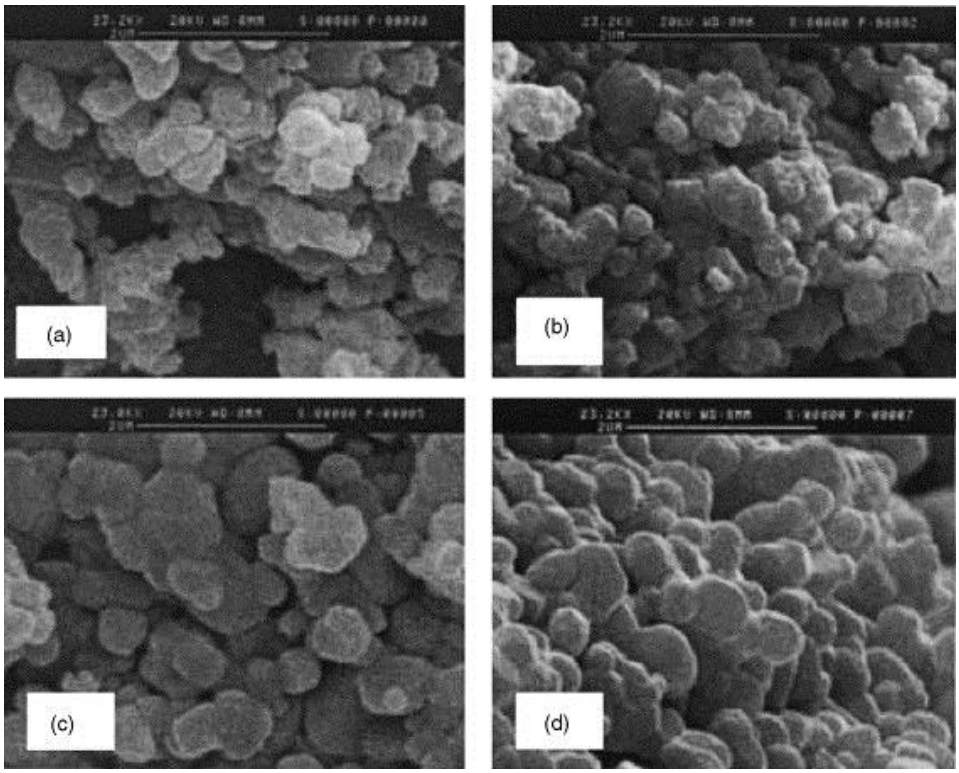

Fig. 7. Typical SEM micrographs of $LiCo_{1-y}Ni_yO_2$ samples annealed at 700 °C. (a) y = 0.4, (b) y = 0.5, (c) y = 0.6 and (d) y = 0.7.

The effect of the synthesis at moderate temperature on the microstructure is clearly depicted when we compare the morphology of powders prepared by the wet-chemical method assisted by citric acid as chelating agent with those prepared by the solid-state reaction (not shown here). The SEM micrographs of the former oxides show that the particles have regular shape with roundness of the edges. The grains are submicron sized in diameter. The wet-chemical synthesis used leads to powder samples having particle size smaller than that of powders prepared at high temperature from solid-state

reaction. Such a behavior is a general trend for samples grown by low-temperature technique. It has been observed for numerous oxides such as lithium cobaltites and lithium manganates [22].

The marked decrease in the particle size of $LiCo_{1-y}Ni_yO_2$ oxides is then unequivocally correlated with kinetics of grain formation using a wet-chemical synthesis assisted by carboxylic acid (Fig. 8). Different possibilities can be considered: (i) conditions under which hydrolysis and condensation of the precursor species take place in a weak acidic medium (pH ≈ 4.5); (ii) fast kinetics of grain formation with the use of glycine; (iii) strong exothermic reaction during the salt decomposition around 320 °C. The homogeneous cations mixing of Li and (Co,Ni) in the initial emulsion favors the tendency of small grains. Since electrochemical lithium intercalation and deintercalation are in general limited by the rate of diffusion, the aforementioned features are important since smaller grain size can favor the lithium-ion mobility in the particles by reducing the ion-diffusion pathway.

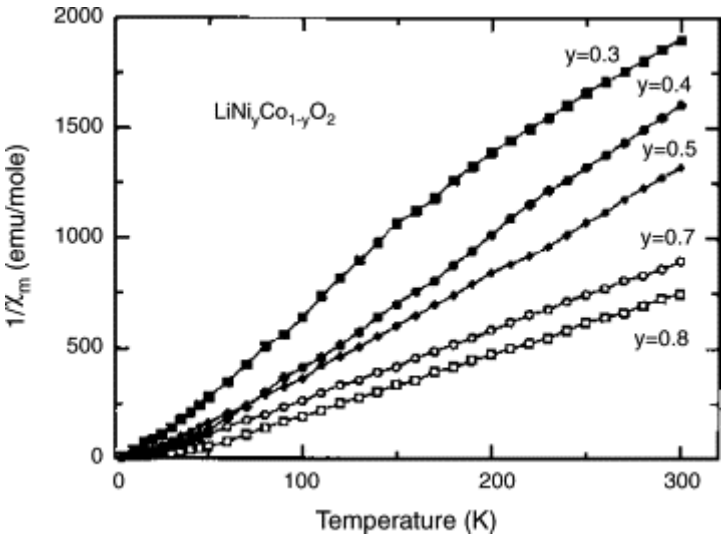

Fig. 8. The temperature dependence of the reciprocal magnetic susceptibilities of the $LiN_{1-y}Co_yO_2$ series measured in the temperature range 4–300 K.

3.3. Magnetic properties

The temperature dependence of the reciprocal magnetic susceptibilities of the $LiNi_{1-y}Co_yO_2$ series measured in the temperature range 4–300 K is shown in Fig. 8. All graphs can be fitted with a Curie–Weiss law in a high temperature range. No shoulder or kink is observed at possible magnetic impurities, such as NiO (T_c = 2000 K) or $Li_{0.5}Ni_{0.5}O$ (T_c = 120 K). The paramagnetic Curie constant, C_p, ranges from 0.13 to 0.32 emu K/mol. The $LiNi_{1-y}Co_yO_2$ compounds exhibit a positive Weiss

temperature, θ_p, in the range 12–29 K which indicates a ferromagnetic interaction of the magnetic centres. Fig. 9 compares the experimental values of C_p with the theoretical ones taking into account the hypothesis of either low- or high-spin state for the M^{3+} ions. As the electronic spin state is different for the Ni^{3+} ($t_{2g}^6 e_g^1$, $S_{LS} = 3/2$, $S_{HS} = 1/2$) and Co^{3+} ($t_{2g}^6 e_g^0$, $S_{LS} = 2$, $S_{HS} = 0$) cations, one expects different evolutions of the Curie constant upon Co substitution in the $LiNi_yCo_{1-y}O_2$ lattice. Theoretical curves are obtained assuming $T >> |\theta_p|$ as followed.

$$p_{\text{eff}}^2 = y p_{\text{eff}(Ni^{3+})}^2 + (1-y) p_{\text{eff}(Co^{3+})}^2,$$

where p_{eff} is the effective number given by $p_{\text{eff}(M^{3+})} = 2\sqrt{S(S+1)}$ with $\mu_{eff} = p_{eff}\mu_B$ (μ_B is the Bohr magneton).

It is clearly demonstrated from data in Fig. 9 that the metal-transition ions are in the low-spin state in the $LiNi_{1-y}Co_yO_2$ solid solution. The ferromagnetic anomalies for $LiNi_{1-y}Co_yO_2$ are probably caused by a small part of the nickel ions at the *3a* sites producing strong magnetic interactions of Ni(3*b*)–O–Ni(3*a*)–O–Ni(3*b*) between different NiO_2 slabs. Accordingly, this type of interaction introduces a three-dimensional magnetic correlation.

3.4. Vibrational spectra

The purpose of this study is to investigate the local environment of cations in a cubic close-packed oxygen array of the $LiCo_{1-y}Ni_yO_2$ lattice using FT-IR spectroscopy. IR-active modes correspond to vibrations involving primarily atomic motion of cations against their oxygen neighbors (Fig. 9). Consequently, these modes are very sensitive to the cationic local environment in the host matrix.

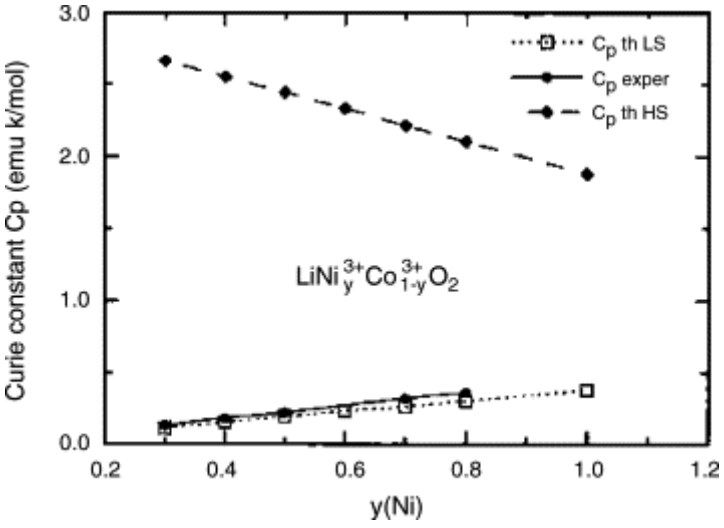

Fig. 9. Variation of the Curie constant determined as a function of the Ni content in the $LiN_{1-}yCoyO_2$ lattice. Theoretical curves for the two types of electronic spin state (HS and LS) are displayed for the determination.

Fig. 10 shows the FT-IR absorption spectra of $LiCo_{0.4}Ni_{0.6}O_2$ powders as a function of the calcination temperature in the range 120–700 °C. FT-IR absorption spectra of $LiCo_{0.4}Ni_{0.6}O_2$ samples display features which can be divided into two parts. (i) The high-wavenumber region of strong absorption corresponds to the broad rock-salt band which has broken into several distinct components at ca. 600–400 cm^{-1}, and (ii) the low-wavenumber region in which an isolated strong band is centered at ca. 240–250 cm^{-1}. It is obviously observed that FT-IR spectra are modified upon calcination. These results are in good agreement with XRD data showing that microcrystalline phases were obtained at 700 °C.

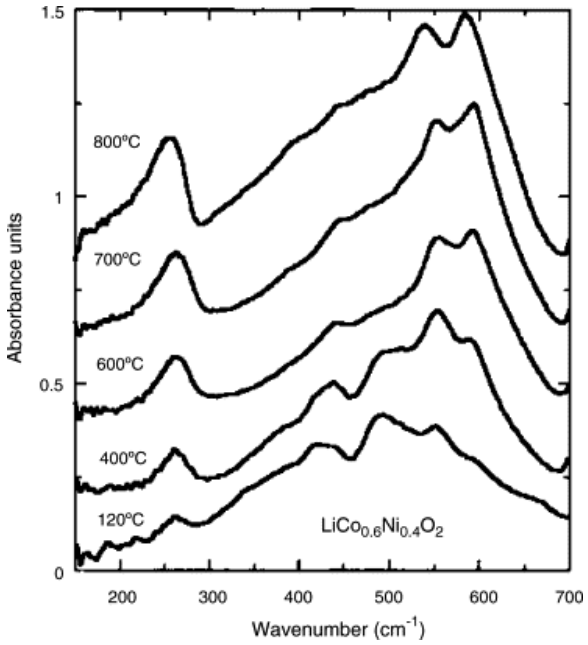

Fig. 10. FT-IR adsorption spectra of $Lico_{1-}yNiyO_2$ powders as a function of the calcinations temperature in the range 120–800 °C.

Layered oxides LiM O_2 possess a crystal structure consisting of alternating layers of trigonally distorted LiO_6 and MeO_6 octahedra sharing edges (O_h local symmetry). It has been shown that $LiCo_{0.4}Ni_{0.6}O_2$ is a solid solution of LiM O_2 (M = Ni, Co) compounds and that stoichiometric $LiCo_{0.4}Ni_{0.6}O_2$ belongs to crystallographic $R\bar{3}m$ space group. The transition-metal cations, i.e. cobalt and nickel, and the lithium ions are located at Wyckoff sites 3b and 3a, respectively, in a cubic close-packed oxygen array. The Li^+ and Co^{III}/Ni^{III} ions are ordered along the (1 1 1) direction of the rock-salt cubic lattice leading to a two-dimensional structure. The ideal layered α-$NaFeO_2$-type structure possesses the spectroscopic D^5_{3d} symmetry with Z = l. Based on the reported crystalline structure of $LiCoO_2$ and using the method of site group analysis, the distribution of the degrees of freedom in irreducible representation was calculated and presented in Table 3 [31], [32] and [33]. For this factor group, four vibrations are infrared-active modes with $2A_{2u}$ + $2E_u$ species. Because FT-IR spectroscopy is capable of probing directly the surrounding environment of the cation, we have studied the local environment of lithium ions in LiM O_2 materials [34],[35] and [36]. It has been also demonstrated that the IR resonant frequencies of alkali metal cations in their octahedral interstices in inorganic oxides are located in the frequency range 200–300 cm^{-1} [37]. Our recent work on transition-metal substitution in LiM O_2 compounds has shown that vibrational mode component of the LiO_6 octahedra appears invariably around 250 cm^{-1} [36]. Thus, the IR resonant frequency of Li–O bonds appears at 269 and 234 cm^{-1} in the $LiCoO_2$ and $LiNiO_2$ layered phases ($R\bar{3}m$ space group), respectively. As far as the low-wavenumber peak is concerned, the isotopic Li replacement in LiMO_2 has proven that this IR band between 200 and 300 cm^{-1} is associated to vibration of the Li–O bonds in LiO_6octahedron [38].

Table 3. Factor group analysis of the LiMO_2-type structures

Atom	Site	Irreducible representation
Li	D_{3d}	$A_{2u} + E_u$
M	D_{3d}	$A_{2u} + E_u$
0	C_{3v}	$A_{1g} + E_g + A_{2u} + E_u$
Total		$A_{lg} + E_g + 3A_{2u} + 3E_u$
Acoustic		$A_{2u} + E_u$
Raman		$A_{lg} + E_g$
Infrared		$2A_{2u} + 2E_u$

Frequencies of the vibrational modes and the analysis of the spectroscopic data of $LiCo_{0.5}Ni_{0.5}O_2$electrode materials are summarized in Table 4. Thus, the vibrational features of $LiCo_{0.5}Ni_{0.5}O_2$microcrystalline powders (calcined at 700–800 °C) are interpreted as follows. The IR band situated at 252 cm^{-1} is assigned with confidence to an asymmetric stretching vibration of the Li^+ ion with O^{2-} near neighbors in $LiCo_{0.5}Ni_{0.5}O_2$. However, a small mixing of Li–O stretching and O–M–O bending motion is present in the low-wavenumber peak. The high-frequency bands of the FT-IR absorption spectra of $LiCo_{0.5}Ni_{0.5}O_2$ located at ca. 575 and 538 cm^{-1} are attributed to the asymmetric stretching modes of MO_6group, whereas the low-frequency bands at ca. 463 and 420 cm^{-1} are assigned to the bending modes of O–M–O chemical bonds.

Table 4. Wavenumber, intensity[a], and assignment of the IR- and Raman-active modes of the layered $LiCo_{0.5}Ni_{0.5}O_2$ compounds calcined at 700 °C for 5 h

Mode	Frequency (cm^{-1})	Intensity[a]	Activity	Assignment	Symmetry
v_1	575	S	IR	$v(MO_6)$	A_{2u}
v_2	566	S	R	$v(MO_6)$	A_{1g}
v_3	538	S	IR	$v(MO_6)$	E_u
v_4	485	m	IR	δ(O–M–O)	E_{uu}
v_5	463	m	R	δ(O–M–O)	E_g
v_6	420	w	IR	δ(O–M–O)	–
v_7	252	S	IR	$v(LiO_6)$	A_{2u}

a S, strong; w, weak; m, medium.

FT-IR measurements on samples calcined at different temperatures confirm XRD data showing the formation of pure phase $LiCo_{1-y}Ni_yO_2$ at 700 °C as shown in Fig. 11. However, we got additional information on the lattice structure, especially on the distribution of the transition metal in the $(Co,Ni)O_2$slabs. The shape of the FT-IR spectrum of sample heated at 700 °C shows the predominance of the stretching modes. The frequency shift of both the stretching and bending modes as a function of the annealing temperature leads to the cationic disorder in the $(Co_{1-y}Ni_y)O_2$ slabs. The frequency shift of the LiO_6 mode has two origins: (i) the slight expansion of the interslab distance (c_{hex} cell parameter) with increasing temperature; (ii) the small mixing of Li–O stretching and O–M–O bending motion present in the low-wavenumber peak. Fig. 12a shows the variation of the frequencies of the high-wavenumber IR-modes with the Co content in $LiCo_{1-y}Ni_yO_2$ oxides. One distinguishes a quasi-linear variation with y, which is the result of the one-mode behavior of the $LiCo_{1-y}Ni_yO_2$ solid solution system. The

evolution of the IR band $v_7$due to the Li–O stretching mode shows the characteristic one-mode behavior with a slight deviation towards low-wavemumber for Ni-rich samples (Fig. 12b). This effect is attributed to the cationic mixing which appears for high content of Ni substitution (y > 0.3).

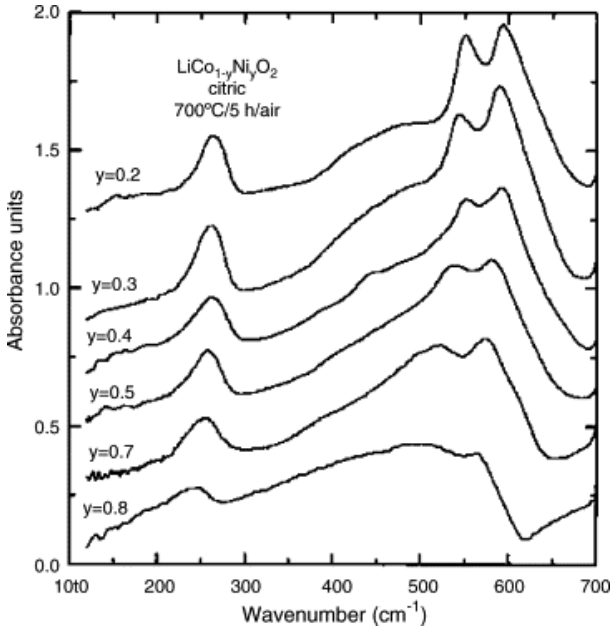

Fig. 11.
FT-IR adsorption spectra of $LiCo_{1-}yNiyO_2$ ($0.2 \leq y \leq 0.8$) microcrystalline powders calcined at 700 °C for 5 h in air.

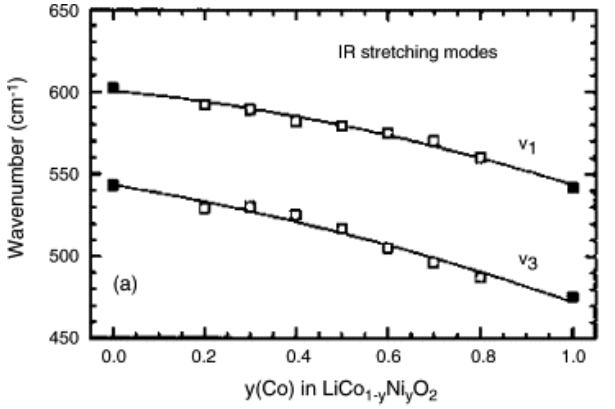

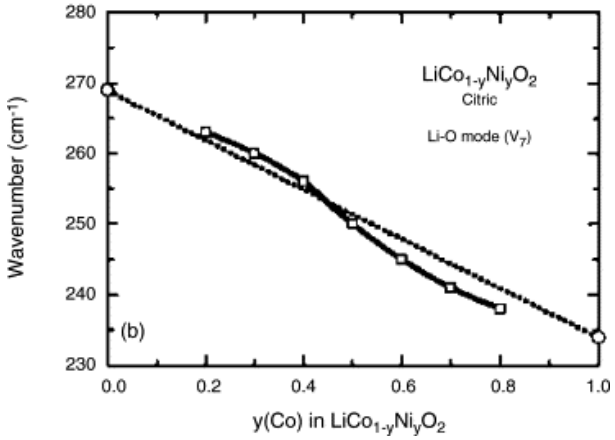

Fig. 12.
Variation of the high-wavenumber IR-mode frequencies as a function of Co content in $LiCo_{1-}yNiyO_2$ oxides. (a) High-wavenumber stretching v_1 and v_3 modes; (b) low-wavenumber v_7 mode. One distinguishes the one-mode behavior of the $LiCo_{1-}yNiyO_2$ solid solution system.

The broadening of the high-wavenumber IR bands may be related with non-homogeneous Ni/Co distribution, variation in the cation–anion bond lengths, and/or polyhedral distortion occurring in $LiCo_{1-y}Ni_yO_2$. It has been reported that the local distortion increases with the decrease of the cobalt concentration in the solid solution [36]. Recording ^7Li NMR spectra of $LiCo_{1-y}Ni_yO_2$ compounds, Delmas and co-workers [39] and [40] have detected slight deviations from a homogeneous Ni/Co distribution and cobalt segregation in the $LiCo_{1-y}Ni_yO_2$ solid solution. It seems that the predominance of the bands in medium-range frequency of the IR spectrum of sol–gel products are due to a local disorder in the $(Co,Ni)O_2$slabs, i.e. non-homogeneous Ni/Co distribution. These results show that FT-IR of $LiCo_{1-y}Ni_yO_2$ materials permits the accurate detection of short-scale heterogeneity complementing the X-ray diffraction analysis which only provides information on the long-range structure.

As a conclusion, our investigations on the vibrational spectra of the $LiCo_{1-y}Ni_yO_2$ oxide compounds have unambiguously determined the layered structure of these materials calcined at 700 °C for 5 h. Analysis of the FT-IR absorption spectra has shown the $R\bar{3}m$ symmetry. It was also demonstrated the local environment of cations against oxygen neighbors, i.e. lithium and transition-metal atoms reside in octahedral interstices of the matrix without cation mixing.

3.5. Electrochemical studies

Electrochemical studies in lithium cells were carried out to compare the performance of low-temperature electrodes $LiCo_{1-y}Ni_yO_2$ prepared by sol–gel method. Electrochemical properties were examined in lithium-containing test cells employing a non-aqueous electrolyte medium. The electrodes are separated by a porous membrane soaked in an electrolyte of 1 M $LiPF_6$ in EC-DMC solvent. The voltage–composition curves of the electrochemical cells using sol–gel $LiCo_{1-y}Ni_yO_2$ cathodes calcined at 700 °C for 5 h is given in Fig. 13. The $Li||LiCo_{1-y}Ni_yO_2$ cells were charged and discharged at current densities of 0.1 mA/cm^2, while the voltage is monitored between 2.5 and 4.2 V using the galvanostatic mode of the MacPile battery tester. These experiments have been carried out at low rates to emphasize the relationship between structure and electrochemistry.

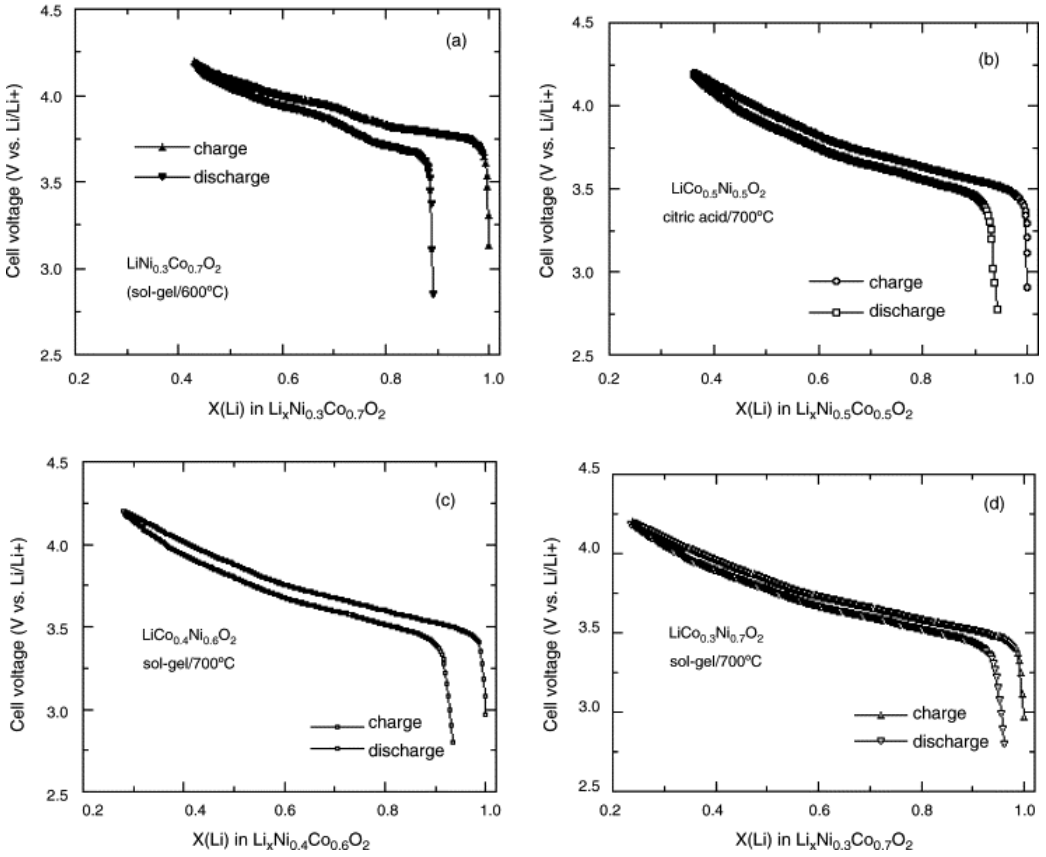

Fig. 13. Typical charge–discharge characteristics of Li||$LiCo_{1-y}Ni_yO_2$ non-aqueous cells (y = 0.3, 0.5, 0.6 and 0.7) using the electrolyte of composition 1 M $LiPF_6$ in EC-DMC at 25 °C. Charge and discharge were obtained at current densities 0.14 mA/cm^2. $LiCo_{1-y}Ni_yO_2$positive electrode materials were calcined at 700 °C for 5 h in air.

In the potential domain 2.5–4.2 V, the charge–discharge curves correspond to the voltage profiles characteristic of the $LiCo_{1-y}Ni_yO_2$ cathode materials associated with lithium occupation of octahedral sites, in agreement with previous works [4], [10] and [15]. However, low-temperature synthesized $LiCo_{1-y}Ni_yO_2$cathode materials showed a lower potential for lithium deintercalation–intercalation than the materials prepared at high temperature, i.e. fired at 800 °C. In the present investigation, similar behavior is also observed on the voltage profiles of the cells using cathodes synthesized by the citric acid-assisted method. It should be remarked that the fully intercalated phases are not recovered during the first discharge. This could be probably assigned to a kinetic problem especially as the $LiCo_{1-y}Ni_yO_2$ phases are poor electronic conductors. However the polarization during both charge and discharge is quite small (<50 mV). These studies also demonstrate that the $LiCo_{1-y}Ni_yO_2$ cathodes yield capacity of about 140 mAh/g when discharged to a cut-off voltage of 2.8 V.

The shape of the charge–discharge curves shows a good reversibility even during the first cycle. In the composition domain $1.00 \geq x \geq 0.45$, the shape of voltage charge profiles of the Li||$LiCo_{1-y}Ni_yO_2$ cells is almost similar to that recorded on high-temperature synthesized materials. Our results of nickel-rich phases are in good agreement with those reported by Ohzuku et al. [4] and by Saadoune and Delmas [10]. The charge potential exhibits a monotonous increase from 3.7 to 4.2 V without appearance of plateau. This evolution comes from the preferential oxidation of Ni^{III} ions even when cobalt ions are substituted for nickel ions in the lattice.

As an example, the lithium extraction/insertion reactions proceed in a $Li_xCo_{0.4}Ni_{0.6}O_2$ matrix having a rhombohedral symmetry. Considering the fully charge state (at 4.2 V, $x = 0.45$), the classical reaction in a Li||$LiCo_{0.4}Ni_{0.6}O_2$ intercalation cell can be written as

$$\square_{0.55}Li_{0.45}[Co_{0.4}^{3+}Ni_{0.55}^{4+}Ni_{0.55}^{3+}]O_2 + 0.55Li^+ + 0.55e^- \leftrightarrow LiCo_{0.4}Ni_{0.6}O_2$$

which normally lies in between the voltage 4.2 and 2.8 V. The layered $Li_xCo_{0.4}Ni_{0.6}O_2$ framework provides a two-dimensional interstitial space for rapid lithium intercalation and deintercalation. It is believed that the *c*-axis of the layered materials expands rapidly on delithiation due to a decrease of the electrostatic binding energy of the lithium-depleted layers [2]. As a concluding remark, it can be pointed out that low-temperature cathode materials exhibit acceptable electrochemical capacity with lower oxidation potential. These compounds are candidates to treat problems due to nickel dioxide formation and electrolyte degradation. This shows the advantage of the soft chemistry synthesis method for $LiCo_{1-y}Ni_yO_2$ preparation, since materials having similar properties can be elaborated in shorter time to reduce the cost of cathode materials.

To formulate the cell potential, we are using the formalism described by Ohzuku et al. [41]. If the energy to put electrons and lithium ions into a triangular lattice is the same, for an intercalation process in which a nearest neighbor interaction is considered, the cell potential can be expressed by

$$V = V_{o,i} - \frac{2RT}{F} \ln\left(\frac{x_i}{1-x_i}\right) - \frac{z\Phi}{F}(1-2x_i),$$

where $V_{o,i}$ is the standard potential, z the number of nearest neighbor sites and Φ is the interaction energy (attractive or repulsive). It should be noted that Eq. (4) may be a

possible statistical thermodynamic origin for lithium ions for both a single-phase ($\Phi < 0$; repulsive interaction) and two-phase ($\Phi > 0$; attractive interaction).

Fig. 14 illustrates the analytical results using Eq. (4) on the quasi-open-circuit voltage for $LiCoO_2$ and $Lix Co_{0.4}Ni_{0.6}O_2$ versus Li/Li^+. Analysis of electrochemical data shows the presence of both two-phase and single-phase region for $LiCoO_2$, while a single-phase region can be solely considered for $LiCo_{1-y}NiyO_2$materials. Both the charge and discharge curve can be described by a single-phase region for $1.0 \geq x \geq 0.42$ with parameters $V_{o,1} = 3.96$ V and $\Phi = -0.21$ V for the charge process and $V_{o,2} = 3.77$ V and $\Phi = -0.29$ V for the discharge curve. This situation is almost identical for the other positive electrode materials. The rechargeability of the $Li||LiCo_{1-y}NiyO_2$ cells appears better than $LiCoO_2$ because the lack of the two-phase behavior in the high-voltage region.

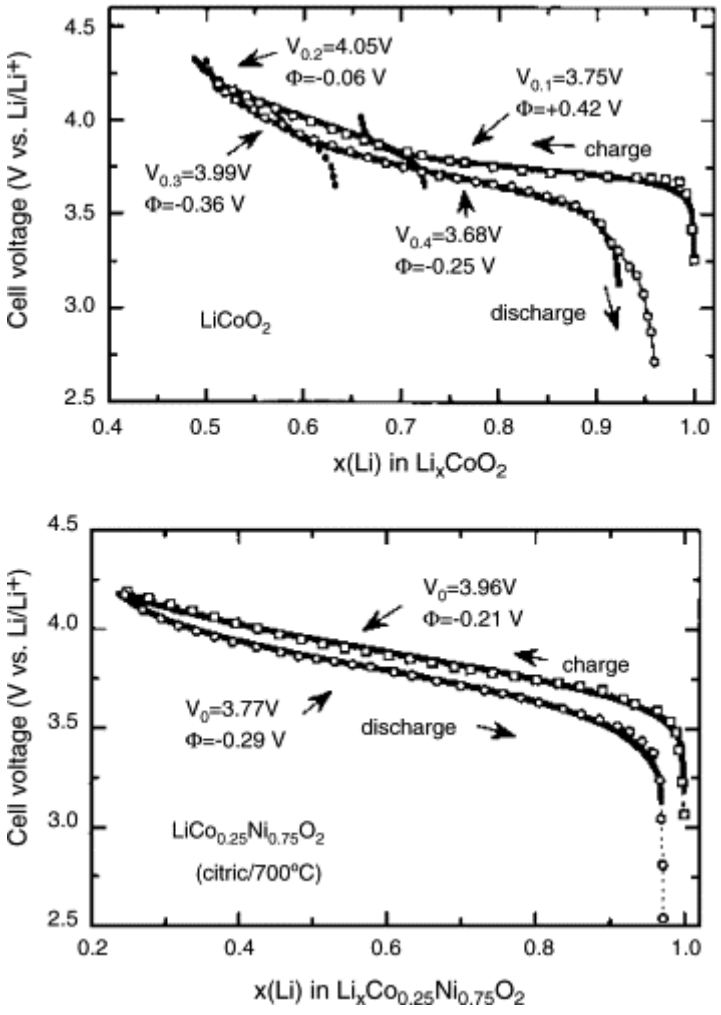

Fig. 14. Typical fits of the charge–discharge for $Li||LiCoO_2$ and $Li||LiCo_{0.25}Ni_{0.75}O_2$ cell profiles using Eq. (4) showing the single-phase and two-phase regions. Dashed and full lines represent the experimental and calculated voltage–composition curves, respectively.

3.6. Lithium ion kinetics

Chemical diffusion coefficients (*D*+) of lithium ions in $LiCo_{1-y}Ni_yO_2$ host materials have been investigated as a function of the amount of lithium deintercalated in the domain of the galvanic cell reversibility. They were determined by the GITT method from the variation of the cell voltage versus time during the relaxation period following a long charge [42]. An estimate of the chemical diffusion coefficient of Li^+ has been elaborated analyzing the semi-infinite diffusion part of the transient voltage

$$D^+ = \frac{4}{\pi}\left(\frac{V_M}{SFz}\right)^2\left[I_0\left(\frac{\partial E}{\partial x}\right)\left(\frac{\partial E}{\partial \sqrt{t}}\right)^{-1}\right]^2,$$

where V_M is the molar volume, S the geometric apparent area, $(\partial E/\partial x)$ the slope of the coulometric titration curve, I_0 the current supplied, and F is the Faraday constant. At any composition, Eq. (5) might satisfy the boundary condition $t \ll L^2/D^+$ [31]. *D*+ was calculated assuming a uniform Li^+ distribution at any composition. Fig. 15 shows the chemical diffusion coefficients of lithium in $Li_xCo_{1-y}Ni_yO_2$ electrode as a function of *x*(Li). From the structural features, it may be inferred that Li^+ diffusion strongly depends on crystal geometry.

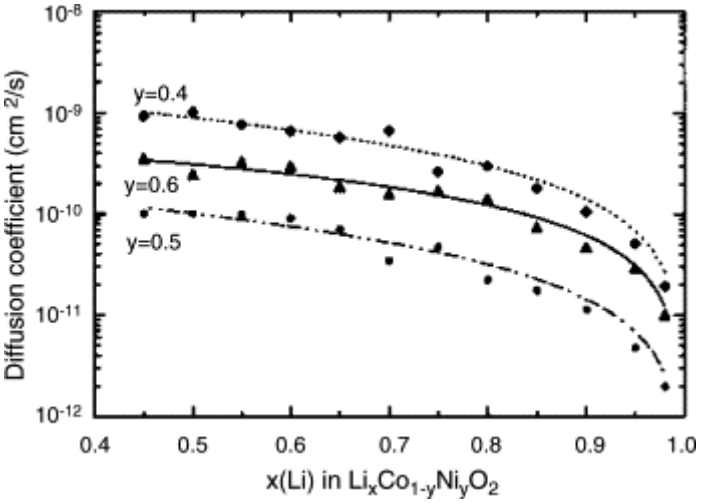

Fig. 15.
Chemical diffusion coefficient of Li ions as a function of the content of lithium deintercalated *x* in $Li_xCo_{1-y}Ni_yO_2$ cathode materials. (a) $y = 0.4$, (b) $y = 0.5$, and (c) $y = 0.6$.

The chemical diffusion coefficients of Li^+ ions in all the $Li_xCo_{1-y}Ni_yO_2$ materials are rather dependent on the degree of lithium deintercalation. Results are as follows. (i) Li^+ ions mobility's in the $Li_xCo_{1-y}Ni_yO_2$structures are quite fast; this should be related to geometrical factors, i.e. octahedral 3a sites of lithium atoms. (ii) Chemical diffusion coefficients of Li^+ in $Li_xCo_{1-y}Ni_yO_2$ increase slightly as lithium is extracted from 1.00 to

0.45. (iii) The rate of diffusion of lithium in LixCo$_{1-y}$NiyO$_2$ cathode materials is in the range $10^{-8}$to 10^{-11} cm^2/s for $0.95 \leq x \leq 0.45$. This can be compared with the data reported for lithium nickel–cobalt oxides [11], [43], [44] and [45]. From a structural point of view, it may be inferred that the layered-like crystal geometry of LixCo$_{1-y}$NiyO$_2$ oxides allows fast Li^+ diffusion.

Based on the lamellar crystal structure of LixCo$_{1-y}$NiyO$_2$ phases, it could be assumed that the motion of Li^+ions is governed by geometrical factors such as the size of the channels which have to be large, and by the degree of covalency of Li–O bonds which has to be low. It is expected that D+ for Li^+ ions would decrease with increasing lithium content owing to a decrease in the number of vacant sites in the host structure. According to our results, it seems that the diffusion of lithium ions through the layered lattice oxides is not influenced by the change of lattice parameter, but by the number of vacant sites available within the lithium layer between (Co,Ni)O$_2$ blocks. In the range of the cell reversibility, LixCo$_{0.4}$Ni$_{0.6}$O$_2$ cathode materials exhibit an increase of more than one order of magnitude in the diffusion coefficients when the cell is charged. The highest values of D+ obtained in LixCo$_{0.4}$Ni$_{0.6}$O$_2$ are attributed to the well-defined 2D structure in this compound.

If we consider that the diffusion of lithium ions into the host lattice has two limiting factors, the ion hopping probability and the degree of occupancy of the sites, then the chemical diffusion coefficient can be expressed as

$$D^+ = k[^2(xm - x) + \beta x(xm - x)],$$

where x_m is the full site occupancy for lithium ions, k the factor related with the probability for ion hopping, and β represents an interaction factor [46]. Dashed line in Fig. 15 is the curve fitted using Eq.(6) giving parameters $k = 1.2 \times 10^{-11}$ cm^2/s and $\beta = 6$ in the compositional range $0.95 \leq x \leq 0.45$ for LixCo$_{0.4}$Ni$_{0.6}$O$_2$. The chemical diffusion coefficient, which is rather dependent on composition, drops up to 1×10^{-8} cm^2/s at $x = 0.65$. This behavior is attributed to the nature of the empty sites in the host structure. The rate capability of Li^+ intercalation materials is often limited by the slow diffusion of Li^+within the solid electrode material. It may then be expected that the layered morphology of the powder could improve diffusion processes at the electrode–electrolyte interface and through the solid phase.

3.7. Cycling

Fig. 16 shows the discharge capacity versus cycle number of Li||$LiCo_{1-y}Ni_yO_2$ cells (y = 0.0, 0.5, 0.6 and 0.7). The $LiCo_{1-y}Ni_yO_2$ electrodes exhibit an initial capacity in the range from 158 to 191 mAh/g for $0.5 \leq y \leq 0.7$. It is obvious that the initial capacity is increased with increasing the Ni content. The electrochemical stability has been attributed to the stronger metal–oxygen bonding in substituted $LiCo_{1-y}Ni_yO_2$ phases. This is also due to the increasing amount of Li^+ ions extracted from $LiCo_{1-y}Ni_yO_2$phase since during the charge process. Obviously, the effect of doping incorporation is a subsequent improvement of the Li||$LiCoO_2$ cell cyclability. The substituted $LiCo_{1-y}Ni_yO_2$ phases are more stable than $LiCoO_2$, and the capacity fading is less for $y \geq 0.4$. The $LiCo_{0.25}Ni_{0.75}O_2$ oxide appears to be the best electrode on cycling which is due to the stabilization of the $LiMO_2$ framework by the Co substitution. The presence of Co^{III} stabilizes the mixed ($Ni_{0.75}Co_{0.25}$) slabs with only trivalent cations. As indicated by FT-IR measurements, a strictly 2D structure is obtained. These electrochemical features show that the capacity of the Li||$LiCo_{0.25}Ni_{0.75}O_2$ cell is decreased 2% of the initial capacity at the 32nd cycle.

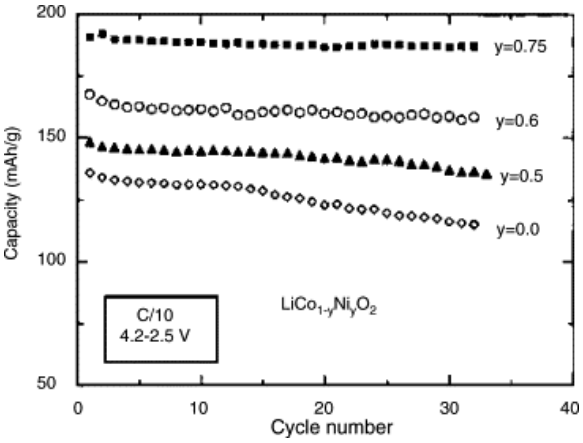

Fig. 16.
Capacity of the Li||$LiCo_{1-y}Ni_yO_2$ cells as a function of the cycle number.

Fig. 17 displays the temperature dependence of the capacity of the Li||$LiCo_{0.25}Ni_{0.75}O_2$ cell operating in the range 2.5–4.2 V. As measured at room temperature, the charge capacity obtained at 60 °C is very close to the initial one. The capacity retention of the electrode is 95% for the 30th cycle. These results show that the elevated temperature does not add complications, such as pronounced surface reactions, massive film formation and consequently, an increase in impedance as found with $LiCoO_2$ at elevated temperatures[47].

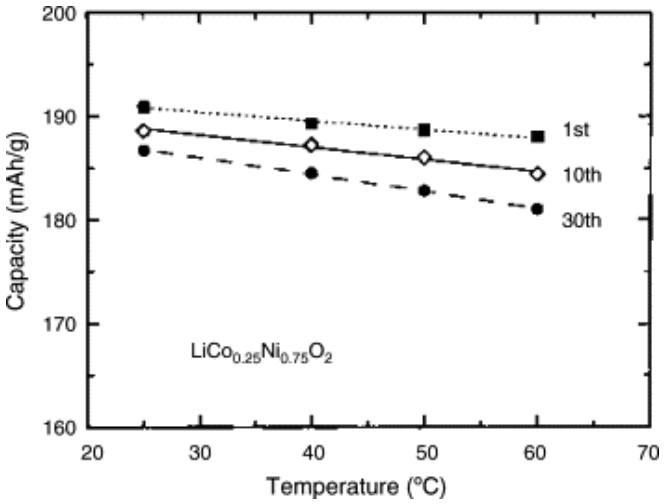

Fig. 17.
Temperature dependence of the capacity of the Li||$LiCo_{0.25}Ni_{0.75}O_2$ cell.

4. Conclusion

This work has shown that impurity free $LiCo_{1-y}Ni_yO_2$ phases can be grown at low temperature using a wet-chemical technique. The citric acid-assisted method provides submicron-sized particles which are welcome for the lithium intercalation–deintercalation reactions occurring in cathode materials for rechargeable lithium cells. The use of solution processing leads to molecular level mixing and highly uniform materials. However, a weak disorder in the cationic sublattice of $LiCo_{1-y}Ni_yO_2$ phases has been detected by FT-IR spectroscopy for $y < 0.3$, which permitted an accurate detection of short-scale heterogeneity complementing the X-ray diffraction analysis. The $LiCo_{1-y}Ni_yO_2$ ($1 - y \geq 0.4$) oxides prepared at 700 °C demonstrate improved electrochemical behavior. The discharge potential curve exhibits monotonous profile from 2.5 to 4.2 V without appearance of any voltage plateau due to the absence of the semiconductor–metal transition. The $LiCo_{0.25}Ni_{0.75}O_2$ electrode prepared by the citric acid-assisted sol–gel method yields a capacity of about 191 mAh/g when discharged to a cut-off voltage of 2.5 V. Charge–discharge cycling tests as a function of temperature show that the elevated temperature does not add complications to the battery.

Acknowledgments

The authors would like to thank Dr. Michel Massot and Dr. Francois Gendron for fruitful discussions. They are grateful to Dr. L. El-Farh for his assistance with sample preparation.

References

1. T. Ohzuku (Ed.), Lithium Batteries, New Materials, Developments and Perspectives, Elsevier, Amsterdam (1993), p. 239

2. R.J. Gummow, M.M. Thackeray
   Solid State Ionics, 53–56 (1992), p. 681

3. C. Delmas, I. Saadoune
   Solid State Ionics, 53–56 (1992), p. 370

4. T. Ohzuku, A. Ueda, M. Nagayama, Y. Iwakoshi, H. Komori
   Electrochim. Acta, 38 (1993), p. 1159

5. E. Zhecheva, R. Stoyanova
   Solid State Ionics, 66 (1993), p. 143

6. C. Delmas, I. Saadoune, A. Rougier
   J. Power Sources, 43/44 (1993), p. 595

7. R.J. Gummow, M.M. Thackeray
   J. Electrochem. Soc., 140 (1993), p. 3365

8. A. Ueda, T. Ohzuku
   J. Electrochem. Soc., 141 (1994), p. 2010

9. A. Rougier, I. Saadoune, P. Gravereau, P. Willmann, C. Delmas
   Solid State Ionics, 90 (1996), p. 83

10. I. Saadoune, C. Delmas
    J. Mater. Chem., 6 (1996), p. 193

11. Y.M. Choi, S.I. Pyun, S.I. Moon
    Solid State Ionics, 89 (1996), p. 43

12. I. Saadoune, M. Menetrier, C. Delmas
    J. Mater. Chem., 7 (1997), p. 2505

13. J.B. Goodenough, D.G. Wickham, W.J. Croft
    J. Phys. Chem. Solids, 5 (1958), p. 107

14. J.N. Reimers, J.R. Dahn
    J. Electrochem. Soc., 139 (1992), p. 2091

15. J. Gummow, D.C. Liles, M.M. Thackeray
    Mater. Res. Bull., 28 (1993), p. 235

16. P. Barboux, J.M. Tarascon, F.K. Shokoohi
    J. Solid State Chem., 94 (1991), p. 185

17. E. Rossen, J.N. Reimers, J.R. Dahn
    Solid State Ionics, 62 (1993), p. 53

18. B. Garcia, P. Barboux, F. Ribot, A. Kahn-Harari, L. Mazerolles, N. Baffier
Solid State Ionics, 80 (1995), p. 111

19. I.-H. Oh, S.-A. Hong, Y.-K. Sun
J. Mater. Sci., 32 (1997), p. 3177

20. J.P. Pereira-Ramos
J. Power Sources, 54 (1995), p. 120

21. J. Livage
Chem. Mater., 3 (1993), p. 578

22. C.J. Brinker, G.W. Scherer
Sol–Gel Science: The Physics and Chemistry of Sol–Gel Processing
Academic Press, London (1990)

23. D. Caurant, N. Baffier, B. Garcia, J.P. Pereira-Ramos
Solid State Ionics, 91 (1996), p. 45

24. Y.S. Lee, Y.K. Sun, K.S. Nahm
Solid State Ionics, 109 (1998), p. 285

25. I.-H. Oh, S.-A. Hong, Y.K. Sun
J. Mater. Sci., 32 (1997), p. 3177

26. H. Taguchi, H. Yoshioka, D. Matsuda, M. Nagao
J. Solid State Chem., 104 (1993), p. 460

27. S. Kumar Saha, A. Pathak, P. Pramanik
J. Mater. Sci. Lett., 14 (1995), p. 35

28. R.D. Shannon
Acta Cryst. A, 32 (1976), p. 751

29. J. Morales, C. Perez-Vicente, J.L. Tirado
Mater. Res. Bull., 25 (1990), p. 623

30. J.R. Dahn, U. von Sacken, C.A. Michael
Solid State Ionics, 44 (1990), p. 87

31. R.K. Moore, W.B. White
J. Am. Ceram. Soc., 53 (1970), p. 679

32. M. Inaba, Y. Todzuka, H. Yoshida, Y. Grincourt, A. Tasaka, Y. Tomida, Z. Ogumi
Chem. Lett., 10 (1995), p. 889

33. W.W. Huang, R. Freeh
Solid State Ionics, 86–88 (1996), p. 395

34. C. Julien, A. Rougier, G.A. Nazri
Mater. Res. Soc. Symp. Proc., 453 (1997), p. 647

35. A. Rougier, G.A. Nazri, C. Julien
Ionics, 3 (1997), p. 170

36. M. Nazri, D. Curtis, B. Yebka, G.A. Nazri, C. Julien
Ext. Abstr. of the 193th Meeting of the Electrochem. Soc., San Diego, CA, May 3–8 (1998)
Abstr. No. 48

37. G.J. Exarhos, W.N. Risen
Solid State Commun., 11 (1970), p. 755

38. P. Tarte, J. Preudhomme
Spectrochim. Acta, 26A (1970), p. 747

39. M. Menetrier, A. Rougier, C. Delmas
Solid State Commun., 90 (1994), p. 439

40. C. Marichal, J. Hirschinger, P. Granger, M. Menetrier, A. Rougier, C. Delmas
Inorg. Chem., 34 (1995), p. 1773

41. T. Ohzuku, K. Nakura, T. Aoki
Electrochim. Acta, 45 (1999), p. 151

42. W. Weppner, R.A. Huggins
J. Electrochem. Soc., 124 (1977), p. 1569

43. M.G.S.R. Thomas, P.G. Bruce, J.B. Goodenough
Solid State Ionics, 17 (1985), p. 13

44. Y.M. Choi, S.I. Pyun, J.S. Bae, S.I. Moon
J. Power Sources, 56 (1995), p. 25

45. F. Croce, A. Deptula, W. Lada, R. Marassi, T. Olczak, F. Ronci
Ionics, 3 (1997), p. 390

46. B. Yebka, C. Julien
Solid State Ionics, 90 (1996), p. 141

47. D. Aurbach, B. Markovsky, E. Levi, A. Rodkin, Y.S. Cohen, M. Schmidt, H.-J. Kim
Electrochim. Acta, 47 (2002), p. 4291